Topological magnetic textures mediated magnetocaloric effect in Janus monolayer

*Weiwei He** *Ziming Tang** *Yan Yin* *Qihua Gong*† *Min Yi* †

W. He, Z. Tang, Y. Yin, Q. Gong, M. Yi
State Key Laboratory of Mechanics and Control for Aerospace Structures & Key Laboratory for Intelligent Nano Materials and Devices of Ministry of Education & Institute for Frontier Science, Nanjing University of Aeronautics and Astronautics (NUAA), Nanjing 210016, China
Email Address: gongqihua@nuaa.edu.cn; yimin@nuaa.edu.cn

Keywords: *Magnetocaloric effect, Janus monolayer, Skyrmion, Meron, Dzyaloshinskii–Moriya interaction*

Topological magnetic textures (TMTs) such as skyrmions, merons and vortices are promising for next-generation spintronic technology. Here, we explore the prospect of TMTs in cooling technology, and specifically elaborate the influence of TMTs on magnetocaloric effect (MCE) in typical Janus monolayers (symmetry-broken VSi_2N_4 derivatives) that exhibit prominent Dzyaloshinskii-Moriya interaction (DMI). It is found that the Janus monolayers $VSi_2N_2P_2$, $VSi_2N_2As_2$ and VSi_2NAs_3 allow for versatile TMTs including bimerons, meron pairs and skyrmions. Skyrmions and bimerons are demonstrated to remain stable up to 100 K. Under external magnetic fields, TMTs either experience shrinkage or exhibit a significant magnetization reversal. This results in TMTs-mediated MCE driven by topological magnetic-to-ferromagnetic phase transition, which intrinsically differs from the conventional MCE driven by paramagnetic-to-ferromagnetic phase transition. The TMTs-mediated MCE is revealed to benefit from a combination of pseudo-first-order and second-order phase transition and thus exhibit a broader operating temperature range. Our findings offer a compelling perspective on the role of TMTs in MCE and highlight the potential of Janus monolayers for micro/nanoscale magnetic cooling technologies.

1 Introduction

Topological magnetic textures (TMTs), including skyrmions [1–3], merons [4–6] and vortices [7–9], have attracted considerable attention since their discovery. These spin configurations typically manifest as isolated particles or periodic lattices and are safeguarded by topological order, enabling their persistent even under tiny thermal fluctuations and slight magnetic field perturbations [10]. TMTs hold significant promise for next-generation spintronic applications due to their unique properties. Unlike conventional magnetic domain walls, skyrmions can be driven by electric currents at much lower current densities [3], making them highly energy-efficient for magnetic storage. Additionally, TMTs contribute to distinct Hall effects, with bimerons enabling the detection of a pure topological Hall effect, free from interference with anomalous or ordinary Hall effects [11]. These characteristics make TMTs not only advantageous for advanced spintronic technologies, but also crucial for the development of low-power racetrack memory and logic circuits [12].

In recent years, magnetic anomalies observed in noncentrosymmetric B20-type chiral magnets, such as MnSi [13–16] and FeGe [17,18], have unveiled new horizons for advancing magnetic cooling technologies. Measurements of magnetization, specific heat, and magnetic susceptibility suggest that abundant spin fluctuations provide freedom degrees in phase space. Due to their manipulability by temperature and magnetic fields, these materials display an extensive variety of spin states, which include helical, conical, skyrmion lattice, fluctuation-disordered, paramagnetic, and field-polarized phases [15]. The entropic signatures accompanying topological magnetic transitions between these phases indicate a significant potential for cooling applications. Theoretical work have further proposed a refrigeration cycle that includes both the skyrmion and ferromagnetic phases,

*Authors contributed equally.
†Corresponding author.

assessing MCE through fractional entropy change [19]. Comparative evaluations of MCE from skyrmion-to-ferromagnetic transitions versus conventional paramagnetic-to-ferromagnetic transitions reveal that the inclusion of skyrmion phases could boost cooling efficiency.

Janus monolayers, which break the spatial centrosymmetry in 2D materials, can effectively induce the Dzyaloshinskii–Moriya interaction (DMI), thereby stabilizing nontrivial TMTs [20,21]. The unique dimensionality and high integration advantages of 2D materials make them an ideal platform for high-density magnetic storage and magnetic cooling applications. However, experimental detection of MCE typically requires measuring magnetization curves or specific heat to infer entropy changes, and the small size of detection probes poses challenges, particularly in 2D material evaluations [22]. As a result, theoretical studies provide an important approach to investigating MCE in 2D topological magnets [23–25]. While some theoretical work has predicted the existence of TMTs in 2D Janus structures [26–30], the influence of these textures on MCE remains unexplored.

In this paper, we investigate the TMTs in 2D VSi_2N_4 derivatives and explore their influence on MCE using multi-scale simulations. The potential for synthesizing VSi_2N_4 derivatives through elemental substitution is confirmed, and the fundamental properties of these Janus magnets are thoroughly examined using *ab-initio* calculations. The key magnetic parameters, such as magnetocrystalline anisotropic energy, magnetic exchange constants, and DMI constants, which are crucial for the formation and stability of TMTs, are determined. Field-cooling simulations reveal that three of VSi_2N_4 derivatives can stably host intrinsic TMTs. The stability of these TMTs under various temperature and magnetic fields is further analyzed. Furthermore, we propose a TMTs-mediated MCE, providing a compelling perspective on the application of TMTs and advancing the potential development of magnetic refrigeration.

2 Results and discussion

2.1 Stability and magnetic properties

Monolayer VSi_2N_4 is primarily constructed from $2H$-MoS_2-type VSi_2 and α-InSe-type Si_2N_2, with its unit cell comprising seven atomic layers arranged in the sequence N–Si–N–V–N–Si–N [31–35]. Within this framework, four nitrogen atoms are substituted by varying numbers of group VA elements, resulting in the formation of two symmetric structures and six asymmetric Janus structures [36], as illustrated in Fig. 1(a). Monolayer VSi_2N_4 belongs to space group 187 ($P\bar{6}m2$) and point group D_{3h}, while the inversion symmetry is broken in the Janus monolayers, thus presenting space group 156 ($P3m1$) and point group C_{3v}. To assess the feasibility of material preparation, energy, phonon and dynamic analyses are conducted before exploring the fundamental properties of Janus monolayers [37, 38]. A thorough stability analysis is provided in Supporting Information. Figures S1-S3 show that only four of the twelve VSi_2N_4 derivatives are anticipated to be stable. For brevity, the -mid suffix of VSi_2N_3P-mid, $VSi_2N_2P_2$-mid, $VSi_2N_2As_2$-mid and VSi_2NAs_3-mid is omitted in the following.

The calculated structural parameters of $VSi_2N_{4-x}Z_x$ monolayers are summarized in Table 1. Janus monolayers VSi_2N_3P, $VSi_2N_2P_2$, $VSi_2N_2As_2$ and VSi_2NAs_3 have optimized lattice constants a of 2.96, 3.13, 3.21 and 3.5 Å,

Table 1: Structural parameters of asymmetric Janus $VSi_2N_{4-x}Z_x$ monolayers, i.e., lattice constant a, magnetic moment per V atom m_V, and band gap E_g.

Materials	a (Å)	m_V (μ_B)	E_g (eV)
VSi_2N_3P-mid	2.96	0.94	–
$VSi_2N_2P_2$-mid	3.13	0.87	–
$VSi_2N_2As_2$-mid	3.21	1.21	–
VSi_2NAs_3-mid	3.50	1.58	–
VSi_2N_4 [39]	2.88	1.03	0.56
VSi_2P_4 [39]	3.48	1.04	0.11
VSi_2As_4 [39]	3.64	1.16	–

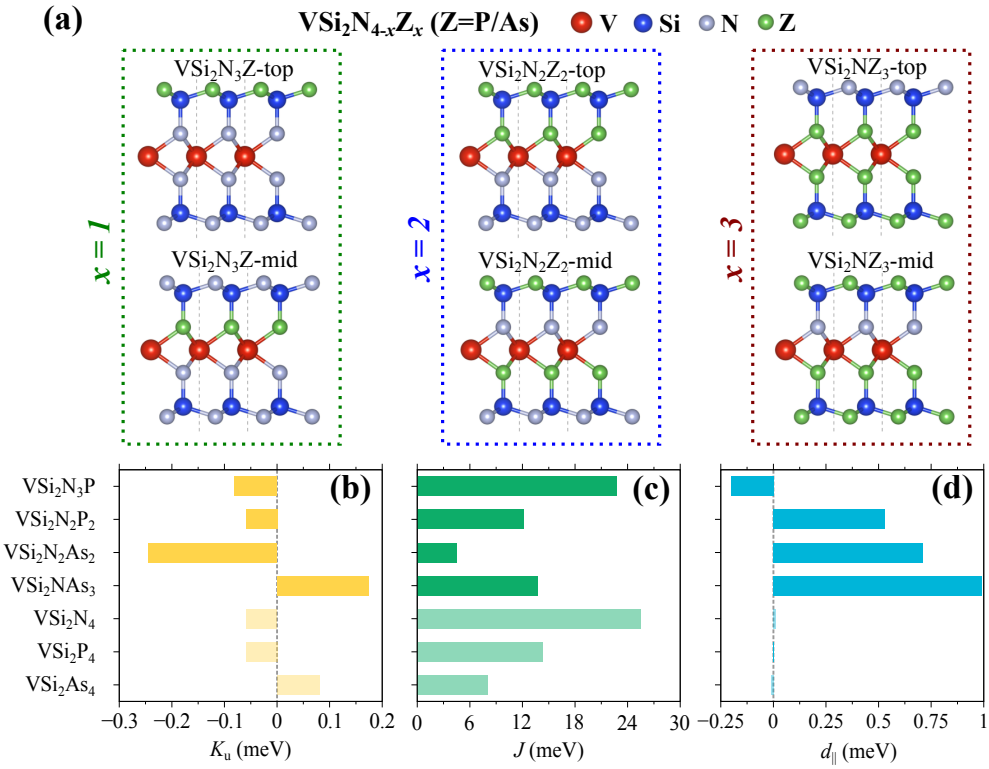

Figure 1: Crystal structures and magnetic properties of asymmetric Janus $VSi_2N_{4-x}Z_x$ ($x = 1, 2, 3$) monolayers. (a) Side views of asymmetric $VSi_2N_{4-x}Z_x$. Red, blue, silver, and green balls represent V, Si, N, and Z (Z=P/As) atoms, respectively. (b) Magnetocrystalline anisotropy energy K_u, (c) exchange interaction constant J, and (d) DMI component $d_{||}$ of Janus monolayers and VSi_2Z_4 (Z=N/P/As). For brevity, the "-mid" suffix is omitted from the four stable Janus structures in (b-d): VSi_2N_3P, $VSi_2N_2P_2$, $VSi_2N_2As_2$ and VSi_2NAs_3.

and magnetic moment per V atom m_V of 0.94, 0.87, 1.21 and 1.58 μ_B, respectively. The band structure of Janus monolayers in Fig. S4 is metallic, whereas VSi_2N_4 and VSi_2P_4 are calculated to be semiconductor [39]. Magnetic parameters such as magnetocrystalline anistropy energy K_u and isotropic exchange parameter J are investigated in $VSi_2N_{4-x}Z_x$ monolayers. Detailed approaches are illustrated in Supporting Information. By breaking symmetric with element replacement, VSi_2N_3P and $VSi_2N_2P_2$ exhibit a weak K_u and a tendency for in-plane magnetization alignment, whereas $VSi_2N_2As_2$ shows a stronger K_u of –0.245 meV, as observed in Fig. 1(b). Distinct from the aforementioned VSi_2N_4 derivatives, VSi_2NAs_3 displays a K_u of 0.173 meV, which may drive the magnetization towards an out-of-plane orientation. As seen in Fig. 1(c), all of VSi_2N_4 derivatives exhibit weaker exchange interactions between V atoms than VSi_2N_4. This reduced interaction strength may result in a lower transition temperature (T_t) from ferromagnetic to paramagnetic phase.

To investigate DMI induced by broken central inversion symmetry in VSi_2N_4 derivatives, we perform spin spiral calculations using the qSO method, as described in the Supporting Information. Previous studies have demonstrated that the spin spiral dispersions are degenerate without spin-orbit coupling (SOC), but become asymmetric when SOC is included [30, 40]. The DMI energy calculated as $\Delta E_{DM}[q] = (E[q] - E[-q])/2$ is subsequently derived. Figure 1(d) displays the in-plane component $d_{||}$ of monolayers, which is derived from Eq. S7. One can see that in VSi_2Z_4 (Z=N/P/As) that preserve their symmetry, $d_{||}$ almost vanishes. On the other hand, there is a corresponding increase in $d_{||}$ values with an elevated substitution by heavier nitrogen group elements. Notably, VSi_2NAs_3 stands out with the largest $d_{||} = 0.99$ meV among the VSi_2N_4 derivatives.

2.2 TMTs and their dynamics

Based on atomic spin model and spin dynamics, we perform zero-field cooling simulations to explore the possible TMTs in Janus VSi_2N_4 derivatives. The relaxed states of 100 nm×100 nm monolayers under zero magnetic field are shown in Fig. 2(a). The magnetization components along specific paths are presented in the bottom-row sub-

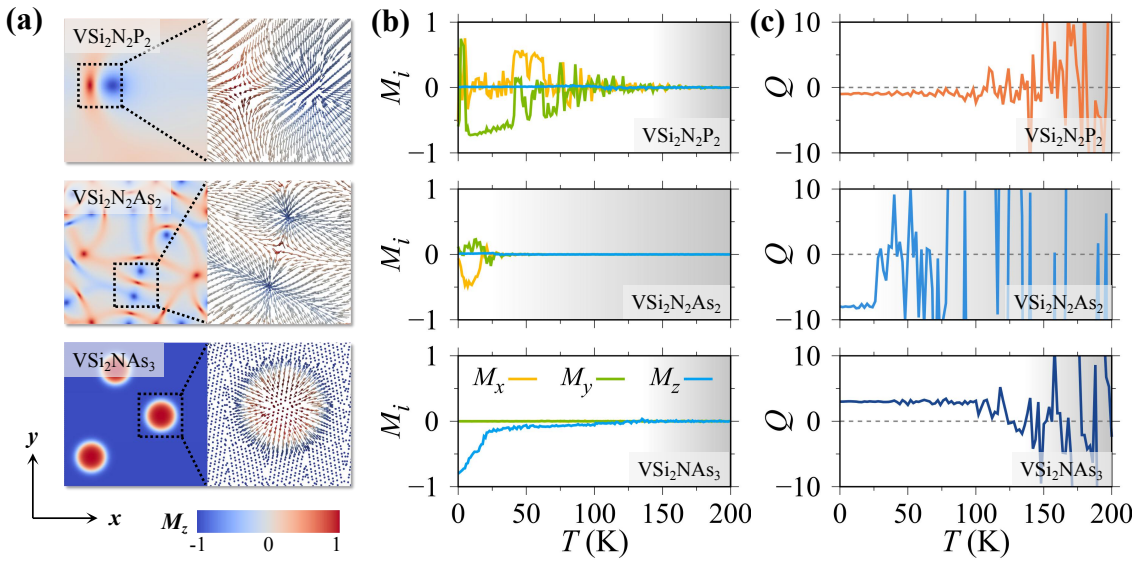

Figure 2: (a) Snapshots of spin dynamics in a periodical nanodisk (100 nm×100 nm) for monolayer $VSi_2N_2P_2$, $VSi_2N_2As_2$ and VSi_2NAs_3, captured after zero-field cooling to 0 K. The red and blue areas correspond to out-of-plane magnetization components $M_z = \pm 1$. The right panels show the magnified magnetic textures framed by a black box to the left. Temperature-dependent (b) magnetization components M_i ($i = x, y, z$) and (c) topological charge Q in VSi_2N_4 derivatives.

figure of Fig. S9. Monolayer $VSi_2N_2P_2$ and $VSi_2N_2As_2$ exhibit bimerons and meron pairs, as shown in Fig. 2(a), with both structures demonstrating in-plane K_u. Figures S9(b) and S9(c) reveal that the out-of-plane magnetization component M_z reaches its maximum only at the meron core (in both positive and negative directions), while elsewhere magnetization predominantly aligns with in-plane direction (either x or y). With a larger DMI/exchange ratio ($|d_\parallel|/J$ =0.158), $VSi_2N_2As_2$ exhibits smaller-sized and higher-density topological structures than $VSi_2N_2P_2$, which has a DMI/exchange ratio of 0.044. Néel-type skyrmions are observed in VSi_2NAs_3, with cores oriented along the $+z$ direction. A moderate DMI/exchange ratio ($|d_\parallel|/J$ =0.072) along with out-of-plane K_u assures the stable existence of skyrmions. It can be seen that the balance between DMI and K_u is critical for maintaining the integrity of TMTs within the VSi_2N_4 derivatives. As depicted in Fig. S9(d), the magnetization components at the skyrmion's periphery show its diameter D as 20 nm. Unlike VSi_2N_4 derivatives that exhibit TMTs, VSi_2N_3P displays a uniform arrangement of in-plane components, as illustrated in Fig. S9(a). This uniformity is primarily attributed to the very weak DMI/exchange ratio ($|d_\parallel|/J < 0.01$), which is insufficient to induce the emergency of TMTs.

To investigate the thermal stability of TMTs, temperature-dependent magnetization components M_i and topological charge Q are examined, as shown in Figs. 2(b) and 2(c). The methodology for calculating Q is comprehensively explained in Supporting Information. Our findings reveal a critical transition temperature T_t that delineates the boundary between topological magnetic (TM) and paramagnetic (PM) states within TMTs. At temperatures surpassing T_t, thermal fluctuations dominate, causing the average magnetization components in all directions to approach zero. Conversely, TMTs are largely preserved below T_t, with the topological charge remaining unchanged. Based on these, T_t value for $VSi_2N_2P_2$, $VSi_2N_2As_2$, and VSi_2NAs_3 are found to be approximately 130, 30 and 150 K, respectively. The temperature-dependent magnetic configurations for TMTs in $VSi_2N_2P_2$ and VSi_2NAs_3 are graphically depicted in Figs. 3(a) and 3(b). These configurations provide a more intuitive representation of the thermal robustness of TMTs. Notably, while TMTs become gradually fuzzy at elevated temperatures, they exhibit remarkable stability up to approximately 100 K in the absence of an external magnetic field.

Furthermore, the effect of external magnetic field on TMTs is explored. As portrayed in Figs 3(a) and 3(b), it is evident that the evolution of TMTs is significantly influenced by the polarity of the applied magnetic field along the same axis. For instance, an increasing magnetic field applied along the $-x$ axis prompts a progressive contraction of bimerons in $VSi_2N_2P_2$ in Fig. 3(a). On the other hand, the magnetization component M_x of bimerons

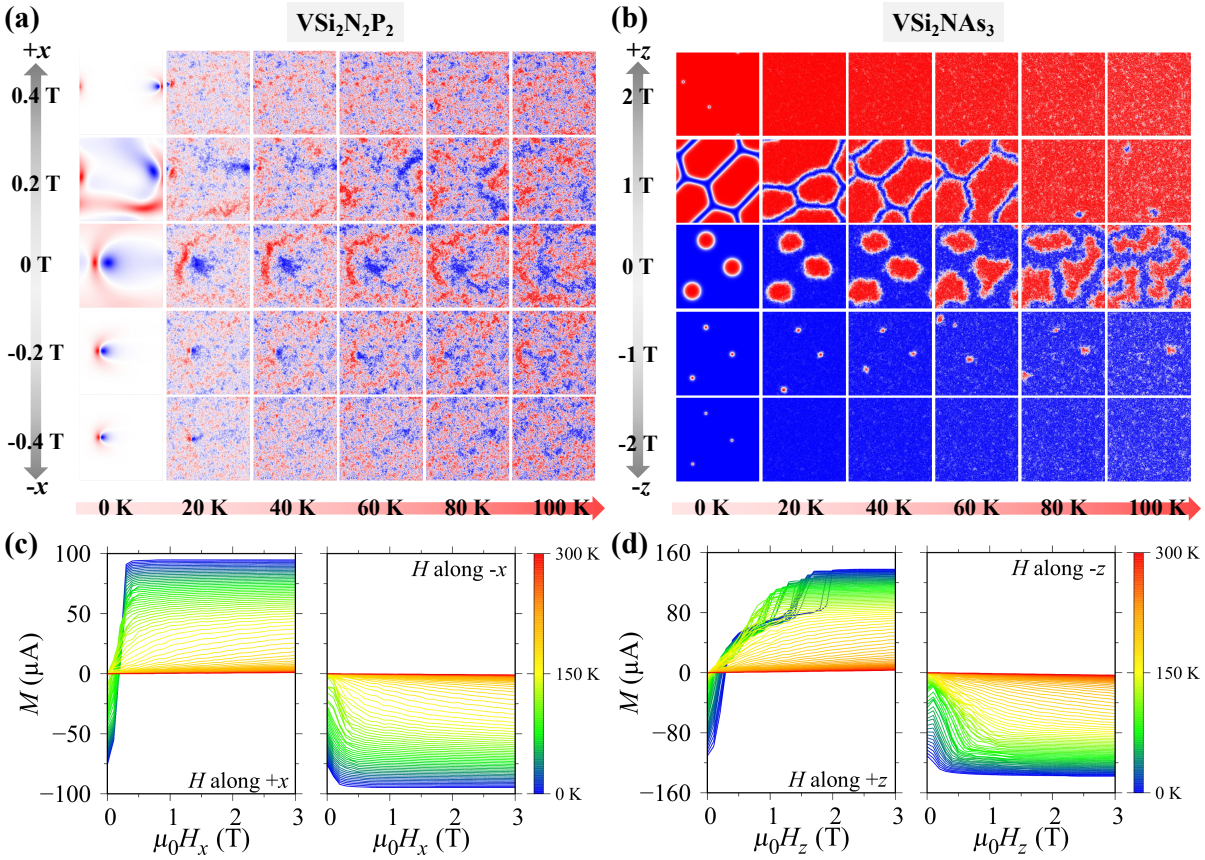

Figure 3: (a, b) Phase of TMTs and (c, d) isothermal magnetization curves for $VSi_2N_2P_2$ and VSi_2NAs_3 across various temperatures and magnetic fields. The red and blue areas correspond to out-of-plane magnetization components $M_z = \pm 1$. $VSi_2N_2P_2$ in (a, c) is investigated under magnetic fields oriented along the $\pm x$-axis, while VSi_2NAs_3 in (b, d) is studied with fields applied along the $\pm z$-axis.

rapidly flips from $-M_x$ to $+M_x$ when the magnetic field is applied along the $+x$ direction, accompanied by a directional movement towards the applied field. Figure 3(b) demonstrates a similar anisotropic responese of TMTs within VSi_2NAs_3. Upon the application of a magnetic field along the $-z$ direction, skyrmions gradually shrink until they eventually disappear. In contrast, the application of a magnetic field along the $+z$ direction initially induces skyrmions to rapidly expand and deform. With sustained magnetic influence, the domain walls squeezed by deformed skyrmions break into smaller isolated skyrmions that eventually annihilate. The anisotropic behavior of TMTs under magnetic fields of different orientations is further elucidated in Figs. 3(c) and 3(d). At low temperatures, magnetization M undergoes a transition from a negative to positive state when the magnetic field is applied along the positive orientation. As the temperature rises, the influence of thermal fluctuations accelerates the transition from TM to PM. Above T_t, M curves dominated by thermal fluctuations show a consistent trend across different magnetic field directions. To summarize, when the magnetic field is applied in a positive direction, $VSi_2N_2P_2$ and VSi_2NAs_3 exhibit more apparent flipping behavior, as seen by M reversal process in Fig. 3. Consequently, subsequent studies primarily focus on situations when the magnetic field is applied in a positive direction.

2.3 TMTs-mediated MCE

We further explore the impact of TMTs on MCE, as shown in Fig. 4. Using M curves, two figures of merit for evaluating MCE, namely the isothermal magnetic entropy change (ΔS_M) and the adiabatic temperature change (ΔT_{ad}), are calculated based on Eqs. 3 and 4. Typically, magnetic cooling is achieved through the MCE driven by the paramagnetic–ferromagnetic (PM–FM) phase transition, as depicted in Fig. 4(a). This conventional MCE does not account for the influence of DMI. When the magnetic field aligns the magnetic spins, a single peak in

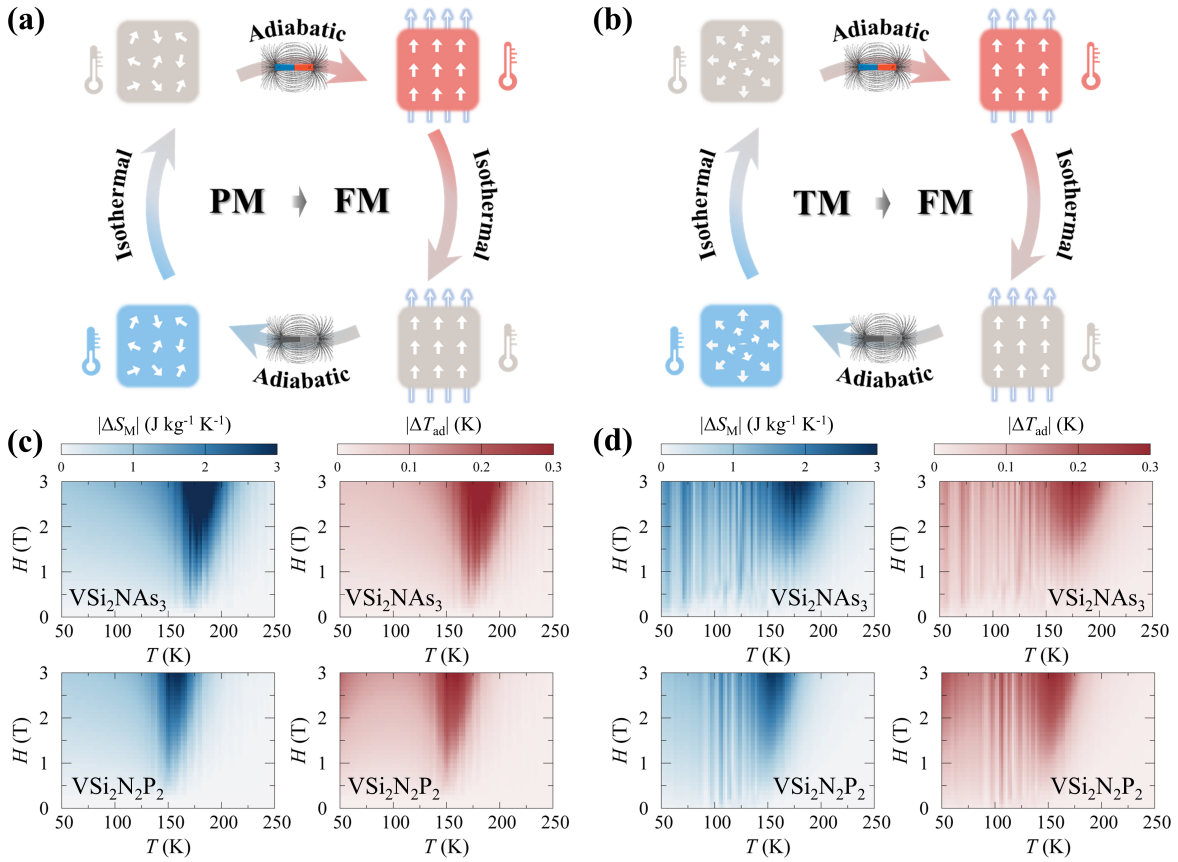

Figure 4: Comparison of conventional MCE driven by the paramagnetic-to-ferromagnetic (PM–FM) phase transition and TMTs-mediated MCE driven by the topological magnetic-to-ferromagnetic (TM–FM) phase transition. (a, b) Schematic of MCE-based magnetic refrigeration cycle. (c, d) Maps of $|\Delta S_M|$ and $|\Delta T_{ad}|$ for $VSi_2N_2P_2$ and VSi_2NAs_3 at different temperatures and magnetic fields.

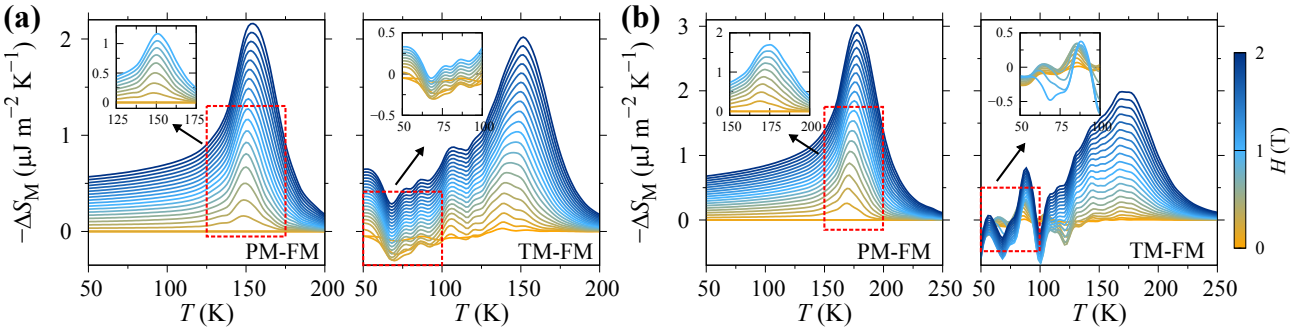

Figure 5: Temperature variation of magnetic entropy change $-\Delta S_M$ for (a) $VSi_2N_2P_2$ with magnetic fields applied along $+x$ direction and (b) VSi_2NAs_3 with fields applied along $+z$ direction. Insets highlight a detail view around the peak of $-\Delta S_M$ curves, corresponding to the phase transition.

$|\Delta S_M|$ and $|\Delta T_{ad}|$ is observed near T_t, as shown in Fig. 4(c). Additionally, the temperature range corresponding to the peak is relatively narrow. These characteristics are consistent with previous studies on conventional MCE in two-dimensional materials [41–44].

For intrinsic TMTs induced by broken inversion symmetry within Janus monolayers, we present a schematic diagram of the magnetic refrigeration cycle based on TMTs-mediated MCE in Fig. 4(b). In this system, the magnetic field drives a topological magnetic-to-ferromagnetic (TM–FM) phase transition by overcoming spin and thermal fluctuations. As shown in Fig. 4(d), the maximum values of $|\Delta S_M|$ and $|\Delta T_{ad}|$ are lower than those in Fig. 4(c). This difference is primarily attributed to the disorder degree within the material. Generally, the entropy of the periodically ordered TM state, which includes skyrmions or merons, is higher than that of the fully polarized FM state but lower than that of the completely disordered PM state. The relationship can be expressed as

$S_{PM} > S_{TM} > S_{FM}$. Compared to conventional MCE, the TMTs-mediated MCE based on TM–FM phase transition exhibits a smaller entropy reduction under the same magnetic field, leading to a decreased peak in $|\Delta S_M|$ and $|\Delta T_{ad}|$. Additionally, working temperature window for TMTs-mediated MCE is significantly broader than that of conventional MCE, as shown in Fig. 4(c). Beyond the peak near T_t, non-negligible values of $|\Delta S_M|$ and $|\Delta T_{ad}|$ are also observed in the low magnetic field region below T_t.

To clarify the phenomena in this region, we plot $-\Delta S_M$ curves under 0–2 T magnetic fields in Fig. 5. The inset of Fig. 5 provides a detailed view of the localized $-\Delta S_M$ curves under 0–1 T magnetic fields. In the conventional second-order phase transition (SOPT), $-\Delta S_M$ curves are continuous and smooth, displaying a single peak near T_t from PM to FM [45]. At sufficiently low temperature, magnetic entropy becomes negligible. In contrast, the TMTs-mediated MCE exhibits a multi-peak trend. As shown in Fig. 5, the peak of $-\Delta S_M$ near T_t reflects the conventional (negative) magnetocaloric behavior of Janus magnets. However, at lower fields and temperatures, the positive entropy change is clearly observed, corresponding to the reversal of M within this region. The fluctuations in $-\Delta S_M$ curves are associated with the formation and annihilation of TM phase, which intuitively manifest as abrupt jumps in M, as shown in Fig. S10. These discontinuous changes at lower fields and temperatures suggest a pseudo-first-order phase transition (FOPT) [19], distinguishing it from the typical second-order phase transition (SOPT) characterized by continuous changes.

Considering Figs. 4 and 5, MCE in Janus magnets with broken symmetry significantly differs from that in 2D magnets with preserved symmetry. Janus magnets featuring TMTs undergo a pseudo-FOPT in the low-temperature and low-field region, while still maintaining the characteristic peak of a SOPT near T_t. The wider operating temperature enhances the potential applications of Janus magnets in magnetic refrigeration, although with a slight reduction in overall magnetocaloric performance.

3 Conclusions

In summary, we have demonstrated TMTs-mediated MCE in typical Janus monolayers (VSi_2N_4 derivatives) that possess notable DMI via multiscale theoretical simulations. In detail, first-principles calculations show that stable Janus structures including $VSi_2N_2P_2$, $VSi_2N_2As_2$ and VSi_2NAs_3 exhibit non-negligible DMI. Atomic spin simulations reveal that these Janus monolayers exhibit intrinsic TMTs without a magnetic field. Specifically, $VSi_2N_2P_2$ hosts bimerons, $VSi_2N_2As_2$ features meron pairs and VSi_2NAs_3 stabilizes skyrmions. By examining the dynamic stability, we find the magnetic field-induced TMTs' evolution is highly polarity-dependent. Based on these findings, we propose a TMTs-mediated refrigeration cycle that is distinct from conventional MCE. Due to the presence of TMTs, the TMTs-mediated MCE shows a pseudo-FOPT at low temperatures and fields. Compared to conventional MCE, the TMTs-mediated MCE offers a wider operating temperature and a unique coexistence of pseudo-FOPT and SOPT. Our work predicts nontrivial TMTs in Janus VSi_2N_4 derived monolayers and elaborates their impact on MCE. These insights enhance the understanding of TMTs in Janus monolayer magnets and pave the way for inspiring innovative magnetic cooling technology by harnessing TMTs.

4 Experimental Section

Ab-initio calculations: The *ab-initio* calculations are conducted using the projector-augmented wave (PAW) method within the Vienna *ab-initio* simulation package (VASP) [46–49]. The exchange-correlation interactions are represented using the generalized gradient approximation (GGA) with the Perdew–Burke–Ernzerhof (PBE) functional [50]. To prevent artificial interactions, a vacuum layer of 30 Å is introduced along the z-axis. The plane-wave cutoff energy is set at 500 eV, with convergence criteria of 10^{-6} eV for energy and 0.001 eV/Å for force. A Monkhorst–Pack k-grid of $15 \times 15 \times 1$ is used to sample the Brillouin zone during ionic relaxation, electronic optimization, and magnetocrystalline anisotropy energy calculations. To accurately account for the

strong correlations of V-3d electrons, the GGA+U method was employed with an effective Hubbard parameter of $U = 2$ eV, as previously discussed in the literature [39]. Further details regarding stability assessments and calculation methods of the magnetic parameters can be found in the Supporting Information.

Atomistic spin simulations: An *ab-initio* informed spin Hamiltonian model is utilized to investigate the dynamics of magnetic spins in Janus monolayers. The Hamiltonian is expressed as

$$H = -\frac{1}{2}\sum_{<i,j>} J(\mathbf{s}_i \cdot \mathbf{s}_j) - \frac{1}{2}\sum_{<i,j>} \boldsymbol{d}_{ij} \cdot (\mathbf{s}_i \times \mathbf{s}_j) - K_u \sum_i (\mathbf{s}_i \cdot \mathbf{e}_i)^2 - \sum_i \mu_s \mathbf{s}_i \cdot (\mathbf{H}_{\text{app}} + \mathbf{H}_{\text{dp}}), \tag{1}$$

where $\mathbf{s}_i$ and $\mathbf{s}_j$ are the spin unit vectors of each atoms at sites i and j, respectively. J and $\boldsymbol{d}_{ij}$ represent the Heisenberg exchange interaction and DMI interaction vector, characterizing the symmetric and asymmetric interactions between two nearest localized spins. K_u, $\mathbf{e}_i$, and μ_s represent the magnetocrystalline anisotropy energy, the easy axis vector, and the magnetic moment at atom i, respectively. $\mathbf{H}_{\text{app}}$ and $\mathbf{H}_{\text{dp}}$ are the external and demagnetization fields, respectively. The magnetic parameters of J, $\boldsymbol{d}_{ij}$, and K_u are derived from *ab-initio* calculations. To address the spatial and temporal evolution of atomic spins under external fields and thermal fluctuations, spin dynamics simulations are utilized to model the behavior of localized magnetic moments. The time-dependent spin direction is governed by the atomistic Landau–Lifshitz–Gilbert (LLG) equation as

$$\frac{\partial \mathbf{s}_i}{\partial t} = -\frac{\gamma}{(1+\lambda^2)}[\mathbf{s}_i \times \mathbf{H}^i_{\text{eff}} + \lambda \mathbf{s}_i \times (\mathbf{s}_i \times \mathbf{H}^i_{\text{eff}})], \tag{2}$$

where the effective field on each spin denoted as $\mathbf{H}^i_{\text{eff}}$ is derived from the spin Hamiltonian as $\mathbf{H}^i_{\text{eff}} = -\partial H/\partial \mathbf{s}_i + \mathbf{H}^i_{\text{th}}$. The fluctuating thermal field $\mathbf{H}^i_{\text{th}}$ is introduced via a Langevin dynamic approach, simulating the interaction of the system with a heat bath. Simulations are conducted on a $100 \times 100 \times 1$ supercell with in-plane periodic boundary conditions. VAMPIRE is used for Monte Carlo and spin dynamics simulations with 100,000 equilibration and 100,000 averaging steps [51, 52]. Additionally, the self-induced demagnetization field due to atomic spins is taken into account, enabling the accurate simulation of temperature-dependent magnetization behavior.

Magnetocaloric thermodynamics: The figures of merit for evaluating MCE, such as the isothermal magnetic entropy change (ΔS_{M}) and the adiabatic temperature change (ΔT_{ad}), can be derived from the first law of thermodynamics and Maxwell's thermodynamic relations [53]. ΔS_{M} is expressed as

$$\Delta S_{\text{M}} = \int_0^H \left(\frac{\partial S}{\partial H}\right)_T \mathrm{d}H = \mu_0 \int_0^H \left(\frac{\partial M}{\partial T}\right)_H \mathrm{d}H, \tag{3}$$

and ΔT_{ad} is given by

$$\Delta T_{\text{ad}} = -\int_0^H \frac{T}{\rho c_{\text{p}}} \left(\frac{\partial S}{\partial H}\right)_T \mathrm{d}H = -\mu_0 \int_0^H \frac{T}{\rho c_{\text{p}}} \left(\frac{\partial M}{\partial T}\right)_H \mathrm{d}H, \tag{4}$$

where S is entropy, M is magnetization, μ_0 is vacuum permeability, H is magnetic field, ρ is the density, and c_{p} is the specific heat capacity.

Supporting Information

Supporting Information is available from the Wiley Online Library or from the author.

Acknowledgements

The authors acknowledge the support from National Natural Science Foundation of China (12272173, 12302134, 11902150), Fundamental Research Funds for the Central Universities (NS2023054, NE2024001), China Postdoctoral Science Foundation (2023M741690), National Youth Talents Program, Research Fund of State Key Laboratory of Mechanics and Control for Aerospace Structures, and a project Funded by the Priority Aca-

demic Program Development of Jiangsu Higher Education Institutions. This work is partially supported by High Performance Computing Platform of Nanjing University of Aeronautics and Astronautics.

Conflict of Interest

The authors declare no conflict of interest.

References

[1] S. Mühlbauer, B. Binz, F. Jonietz, C. Pfleiderer, A. Rosch, A. Neubauer, R. Georgii, P. Böni, *Science* **2009**, *323*, 5916 915.

[2] S. Heinze, K. Von Bergmann, M. Menzel, J. Brede, A. Kubetzka, R. Wiesendanger, G. Bihlmayer, S. Blügel, *Nature Physics* **2011**, *7*, 9 713.

[3] A. Fert, V. Cros, J. Sampaio, *Nature Nanotechnology* **2013**, *8*, 3 152.

[4] S.-Z. Lin, A. Saxena, C. D. Batista, *Physical Review B* **2015**, *91* 224407.

[5] X. Z. Yu, W. Koshibae, Y. Tokunaga, K. Shibata, Y. Taguchi, N. Nagaosa, Y. Tokura, *Nature* **2018**, *564* 95.

[6] M. Augustin, S. Jenkins, R. F. Evans, K. S. Novoselov, E. J. Santos, *Nature Communications* **2021**, *12* 185.

[7] T. Shinjo, T. Okuno, R. Hassdorf, □. K. Shigeto, T. Ono, *Science* **2000**, *289*, 5481 930.

[8] X. Fu, S. D. Pollard, B. Chen, B.-K. Yoo, H. Yang, Y. Zhu, *Science Advances* **2018**, *4*, 7 eaat3077.

[9] J. Sun, S. Shi, J. Wang, *Physical Review Letters* **2023**, *130*, 25 256701.

[10] H. Yoshimochi, R. Takagi, J. Ju, N. D. Khanh, H. Saito, H. Sagayama, H. Nakao, S. Itoh, Y. Tokura, T. Arima, S. Hayami, T. Nakajima, S. Seki, *Nature Physics* **2024**, *20*, 6 1001.

[11] B. Göbel, A. Mook, J. Henk, I. Mertig, O. A. Tretiakov, *Physical Review B* **2019**, *99*, 6 060407.

[12] S. Li, W. Kang, X. Zhang, T. Nie, Y. Zhou, K. L. Wang, W. Zhao, *Materials Horizons* **2021**, *8*, 3 854.

[13] C. Pappas, E. Lelièvre-Berna, P. Falus, P. M. Bentley, E. Moskvin, S. Grigoriev, P. Fouquet, B. Farago, *Physical Review Letters* **2009**, *102* 197202.

[14] M. Janoschek, M. Garst, A. Bauer, P. Krautscheid, R. Georgii, P. Böni, C. Pfleiderer, *Physical Review B - Condensed Matter and Materials Physics* **2013**, *87*, 13 134407.

[15] A. Bauer, M. Garst, C. Pfleiderer, *Physical Review Letters* **2013**, *110*, 17 177207.

[16] J. Kindervater, I. Stasinopoulos, A. Bauer, F. X. Haslbeck, F. Rucker, A. Chacon, S. Mühlbauer, C. Franz, M. Garst, D. Grundler, C. Pfleiderer, *Physical Review X* **2019**, *91*, 4 41059.

[17] H. Wilhelm, M. Baenitz, M. Schmidt, U. K. Rößler, A. A. Leonov, A. N. Bogdanov, *Physical Review Letters* **2011**, *107* 127203.

[18] J. D. Bocarsly, R. F. Need, R. Seshadri, S. D. Wilson, *Physical Review B* **2018**, *97*, 10 100404.

[19] A. R. Saikia, N. Mohanta **2024**, 1–8.

[20] J. Jiang, W. Mi, *Materials Horizons* **2022**, *10*, 3 788.

[21] Y. Yin, Q. Gong, M. Yi, W. Guo, *Advanced Functional Materials* **2023**, *33*, 26 2214050.

[22] Z. WEI, J. LIU, Y. OUYANG, Y. SHEN, F. CHEN, Y. JIANG, *SCIENTIA SINICA Physica, Mechanica & Astronomica* **2021**, *51*, 6 067504.

[23] V. V. Sokolovskiy, O. N. Miroshkina, V. D. Buchelnikov, *Physics of Metals and Metallography* **2022**, *123*, 4 319.

[24] K. Dou, Z. He, W. Du, Y. Dai, B. Huang, Y. Ma, *Advanced Functional Materials* **2023**, *33*, 28 2301817.

[25] H. Yang, J. Liang, Q. Cui, *Nature Reviews Physics* **2023**, *5* 43.

[26] Q. Cui, J. Liang, Z. Shao, P. Cui, H. Yang, *Physical Review B* **2020**, *102*, 9 094425.

[27] J. Jiang, X. Liu, R. Li, W. Mi, *Applied Physics Letters* **2021**, *119*, 7 072401.

[28] K. Dou, W. Du, Z. He, Y. Dai, B. Huang, Y. Ma, *ACS Nano* **2022**, *17* 1144.

[29] W. Du, K. Dou, Z. He, Y. Dai, B. Huang, Y. Ma, *Nano Letters* **2022**, *22*, 8 3440.

[30] P. Li, D. Yu, J. Liang, Y. Ga, H. Yang, *Physical Review B* **2023**, *107*, 5 54408.

[31] Y. Yin, M. Yi, W. Guo, *ACS Applied Materials & Interfaces* **2021**, *13*, 38 45907.

[32] Q. Cui, Y. Zhu, J. Liang, P. Cui, H. Yang, *Physical Review B* **2021**, *103* 085421.

[33] Z. Zhao, X. Duan, X. Fang, X. Wang, W. Mi, *Applied Surface Science* **2023**, *611* 155693.

[34] L. Qiao, M. Li, Y. Cui, S. Xu, J. R. Reimers, W. Ren, *Nano Letters* **2024**, *24*, 21 6403.

[35] Y. Yin, W. He, W. Tang, M. Yi, *Advanced Quantum Technologies* **2024**, 2400391.

[36] Y. Yin, Q. Gong, M. Yi, W. Guo, *Materials Horizons* **2023**, *10* 5177.

[37] O. I. Malyi, K. V. Sopiha, C. Persson, *ACS Applied Materials & Interfaces* **2019**, *11* 24876.

[38] A. Yadav, C. M. Acosta, G. M. Dalpian, O. I. Malyi, *Matter* **2023**, *6*, 9 2711.

[39] W. He, Y. Yin, Z. Tang, X. Wang, H. Yuan, Q. Gong, M. Yi, *Applied Physics Letters* **2024**, *125*, 2 022407.

[40] J. Liang, Q. Cui, H. Yang, *Physical Review B* **2020**, *102*, 22 220409.

[41] M. Xue, W. He, Q. Gong, M. Yi, W. Guo, *Extreme Mechanics Letters* **2022**, *57* 101900.

[42] W. He, Y. Yin, Q. Gong, R. F. Evans, O. Gutfleisch, B. Xu, M. Yi, W. Guo, *Small* **2023**, *19*, 36 2300333.

[43] W. He, Z. Tang, Q. Gong, M. Yi, W. Guo, *SCIENCE CHINA Physics, Mechanics & Astronomy* **2024**, *67* 226811.

[44] L. Patra, Y. Quan, B. Liao, *Journal of Applied Physics* **2024**, *136* 024301.

[45] H. B. Tran, H. Momida, Y. ichiro Matsushita, K. Shirai, T. Oguchi, *Acta Materialia* **2022**, *231* 117851.

[46] P. E. Blöchl, *Physical Review B* **1994**, *50* 17953.

[47] G. Kresse, J. Furthmüller, *Computational Materials Science* **1996**, *6*, 1 15.

[48] G. Kresse, J. Furthmüller, *Physical Review B* **1996**, *54* 11169.

[49] G. Kresse, D. Joubert, *Physical Review B* **1999**, *59* 1758.

[50] J. P. Perdew, K. Burke, M. Ernzerhof, *Physical Review Letters* **1996**, *77* 3865.

[51] R. F. Evans, W. J. Fan, P. Chureemart, T. A. Ostler, M. O. Ellis, R. W. Chantrell, *Journal of Physics: Condensed Matter* **2014**, *26*, 10 103202.

[52] Q. H. Wang, A. Bedoya-Pinto, M. Blei, A. H. Dismukes, A. Hamo, S. Jenkins, M. Koperski, Y. Liu, Q. C. Sun, E. J. Telford, H. H. Kim, M. Augustin, U. Vool, J. X. Yin, L. H. Li, A. Falin, C. R. Dean, F. Casanova, R. F. Evans, M. Chshiev, A. Mishchenko, C. Petrovic, R. He, L. Zhao, A. W. Tsen, B. D. Gerardot, M. Brotons-Gisbert, Z. Guguchia, X. Roy, S. Tongay, Z. Wang, M. Z. Hasan, J. Wrachtrup, A. Yacoby, A. Fert, S. Parkin, K. S. Novoselov, P. Dai, L. Balicas, E. J. Santos, *ACS Nano* **2022**, *16*, 5 6960.

[53] V. Franco, J. Blázquez, J. Ipus, J. Law, L. Moreno-Ramírez, A. Conde, *Progress in Materials Science* **2018**, *93* 112.

Supplementary Information

Topological magnetic textures mediated magnetocaloric effect in Janus monolayer

Weiwei He,[†,‡] Ziming Tang,[†,‡] Yan Yin,[†] Qihua Gong,[*,†] and Min Yi[*,†]

†*State Key Laboratory of Mechanics and Control for Aerospace Structures & Key Laboratory for Intelligent Nano Materials and Devices of Ministry of Education & Institute for Frontier Science, Nanjing University of Aeronautics and Astronautics (NUAA), Nanjing 210016, China*

‡*Authors contributed equally.*

E-mail: gongqihua@nuaa.edu.cn; yimin@nuaa.edu.cn

Stability of Janus monolayers

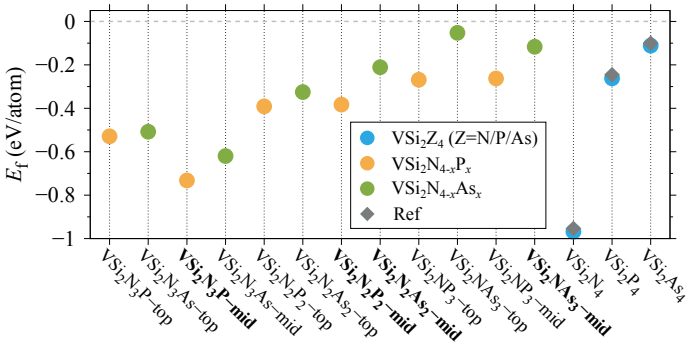

Figure S1: Formation energy E_f of VSi_2Z_4 (Z=N/P/As) and VSi_2N_4 derivatives. E_f of VSi_2Z_4 is from Ref.[4]

The formation energy E_f of Janus monolayers is calculated as $E_f = (E_{VSi_2N_{4-x}Z_x} - E_V - 2E_{Si} - (4-x)E_N - xE_Z)/7$, where $E_{VSi_2N_{4-x}Z_x}$ represents the total energy of $VSi_2N_{4-x}Z_x$, and E_V, E_{Si}, E_N, and E_Z denote the ground state energies of single atoms in their respective elemental crystals. As demonstrated in Fig. S1, the E_f values for monolayer VSi_2Z_4 (Z=N/P/As) closely align with those reported in previous work.[4] All twelve Janus monolayers with negative E_f are energetically stable. Moreover, the phonon and dynamic stabilities of Janus monolayers are examined through phonon spectra calculations and *ab-initio* molecular dynamics (AIMD) simulations. The results of phonon spectra and AIMD simulations are provided in Figs. S2 and S3. Among them, phonon frequencies of VSi_2N_3P-mid, $VSi_2N_2P_2$-mid, $VSi_2N_2As_2$-mid, and VSi_2NAs_3-mid are almost positive, indicating phonon stability. The evolution of total energy and structure snapshots, captured at the end of 10 ps AIMD simulations, confirming their thermal stability up to room temperature (300 K).

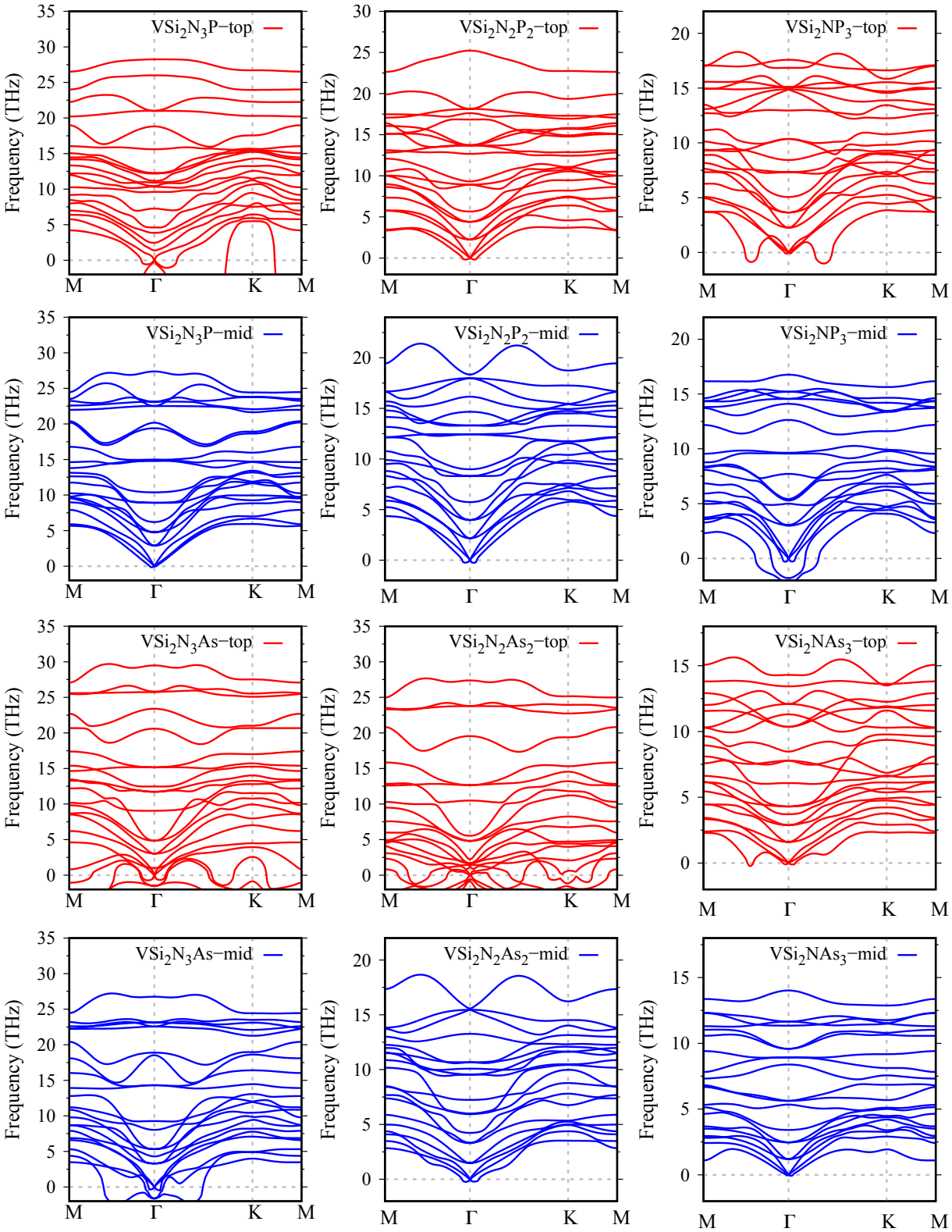

Figure S2: Phonon dispersion spectra of monolayer VSi_2N_4 derivatives.

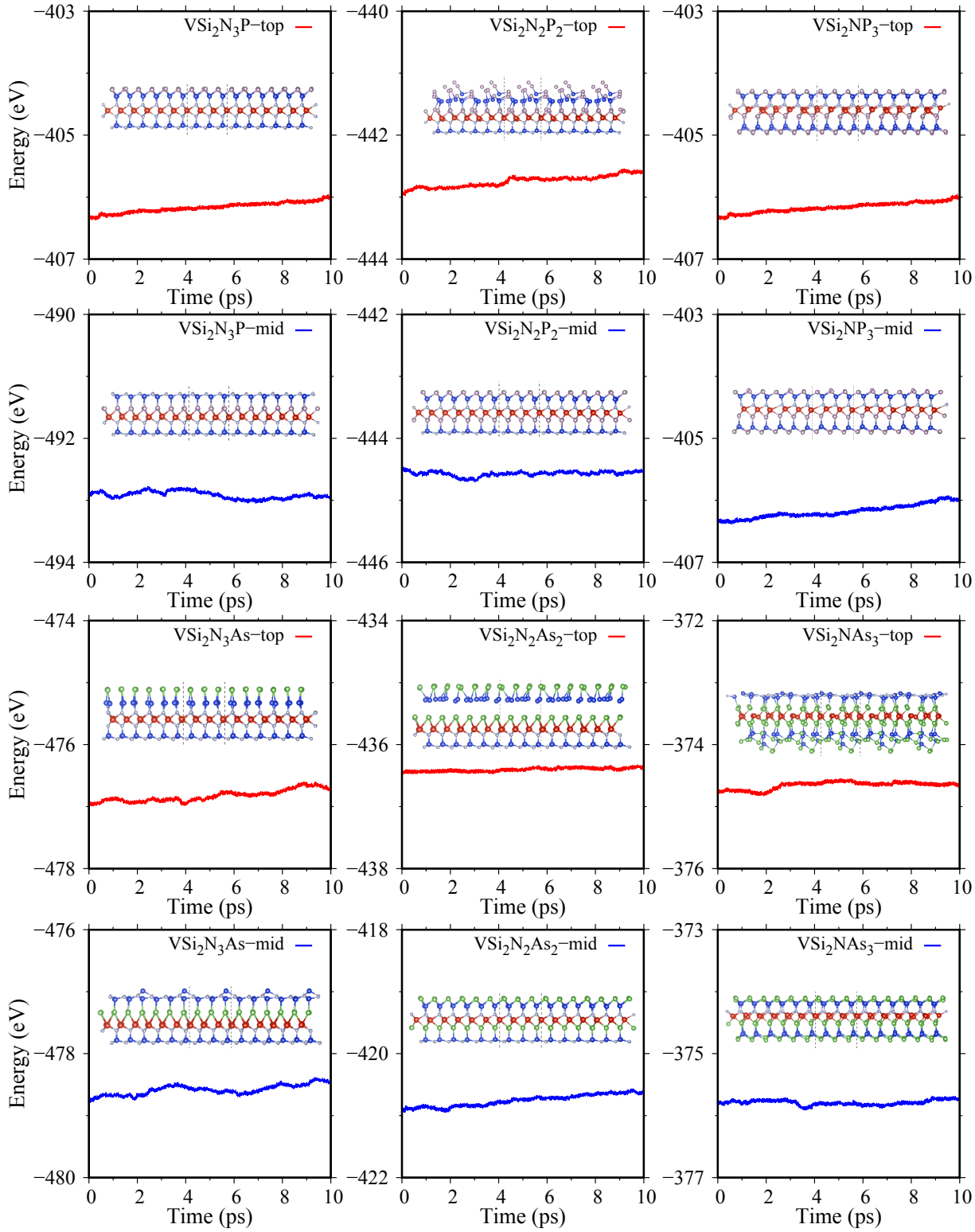

Figure S3: Variation of total energy with time by *ab-initio* molecular dynamics (AIMD) simulation of monolayer VSi_2N_4 derivatives and its corresponding snapshot taken from the end of the simulations. The AIMD simulation within the NVT is implemented to calculate the $3 \times 3 \times 1$ supercells at 300 K.

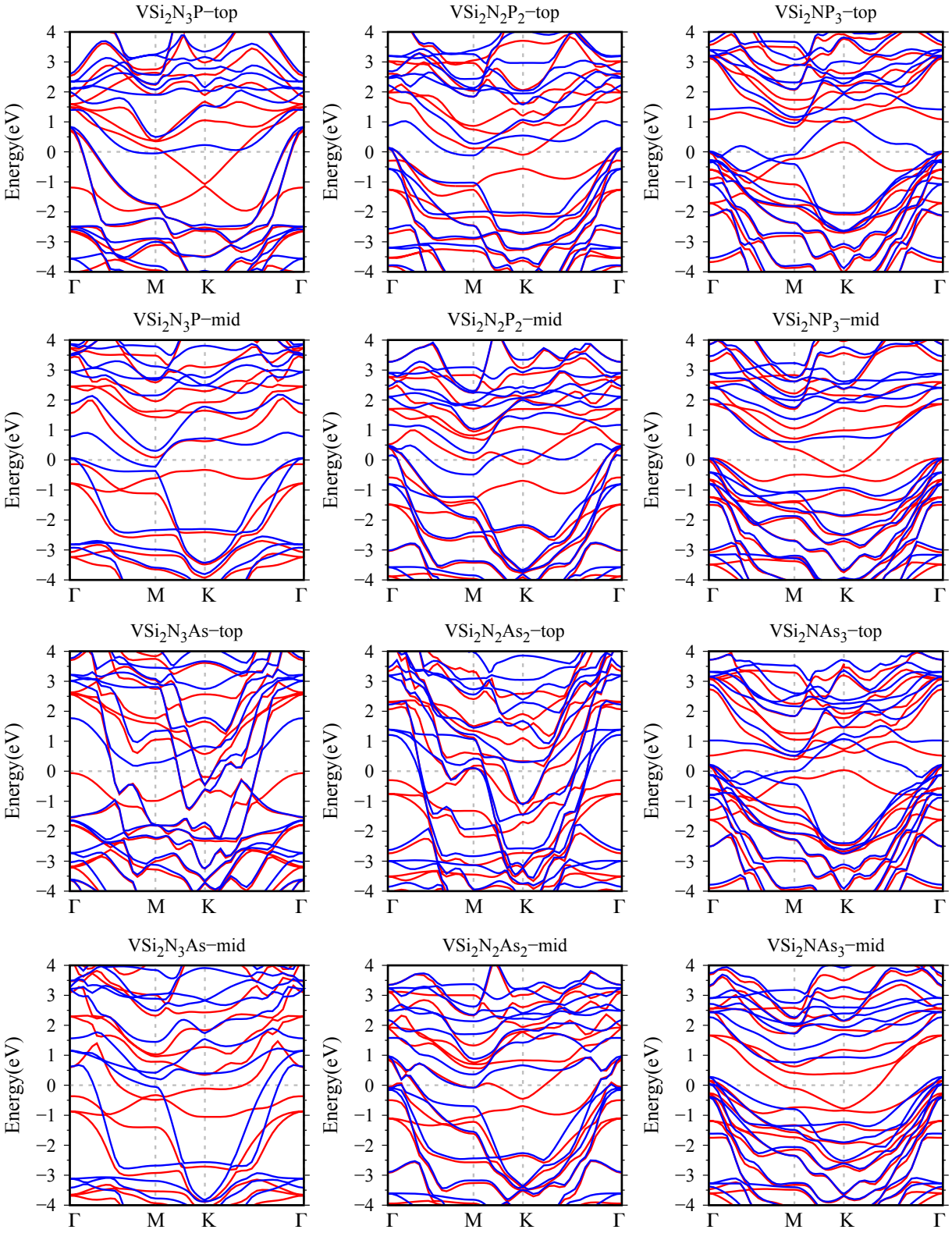

Figure S4: The spin-polarized band structures of monolayer VSi_2N_4 derivatives. The red (blue) lines represent spin-up (spin-down) bands.

Calculation methods of K_{u}, J and $d_{\|}$

The *ab-initio* calculations are conducted using the projector-augmented wave (PAW) method within the Vienna *ab-initio* simulation package (VASP).[5–8] The exchange-correlation interactions are represented using the generalized gradient approximation (GGA) with the Perdew–Burke–Ernzerhof (PBE) functional.[9] To prevent artificial interactions, a vacuum layer of 30 Å is introduced along the z-axis. The plane-wave cutoff energy is set at 500 eV, with convergence criteria of 10^{-6} eV for energy and 0.001 eV/Å for force. A Monkhorst–Pack k-grid of $15 \times 15 \times 1$ is used to sample the Brillouin zone during ionic relaxation, electronic optimization, and magnetocrystalline anisotropy energy calculations. To accurately account for the strong correlations of V-3d electrons, the GGA+U method was employed with an effective Hubbard parameter of $U = 2$ eV, as previously discussed in the literature.[10]

To obtain the magnetic exchange constant J, we calculate the collinear spin configurations as shown in Fig. S5 with a $1 \times \sqrt{3} \times 1$ supercell and a $16 \times 9 \times 1$ k-point mesh. The total energies for ferromagnetic and antiferromagnetic spin configurations are given as follow:

$$E_{FM} = E_0 - 6J, \tag{S1}$$

$$E_{AFM} = E_0 + 2J, \tag{S2}$$

in which E_0 is the energy independent of spin. Then the J can be solved as $J = (E_{AFM} - E_{FM})/8$.

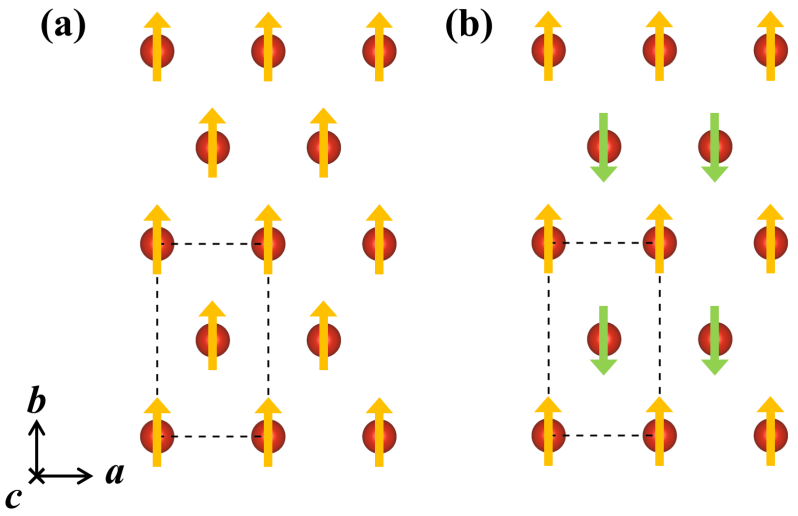

Figure S5: Schematic diagram of (a) ferromagnetic and (b) antiferromagnetic spin configurations within monolayer VSi_2N_4 derivatives.

We perform the noncollinear non-self-consistent calculations with spin-orbit coupling to calculate the total energy difference when the spin quantization axis are aligned along different crystallographic axes, the magnetocrystalline anistropy energy K_{u} is obtained as follows:

$$K_{\mathrm{u}} = E_{[100]} - E_{[001]}, \tag{S3}$$

where $E_{[100]}/E_{[001]}$ represents the energy when the magnetization aligns in the in-plane/out-of-plane orientation.

The total Dzyaloshinskii-Moriya interaction (DMI) energy in Janus VA_2Z_4 monolayers can be written as

$$E_{\mathrm{DM}} = -\sum_{\langle i,j \rangle} \boldsymbol{d}_{ij} \cdot (\boldsymbol{S}_i \times \boldsymbol{S}_j), \tag{S4}$$

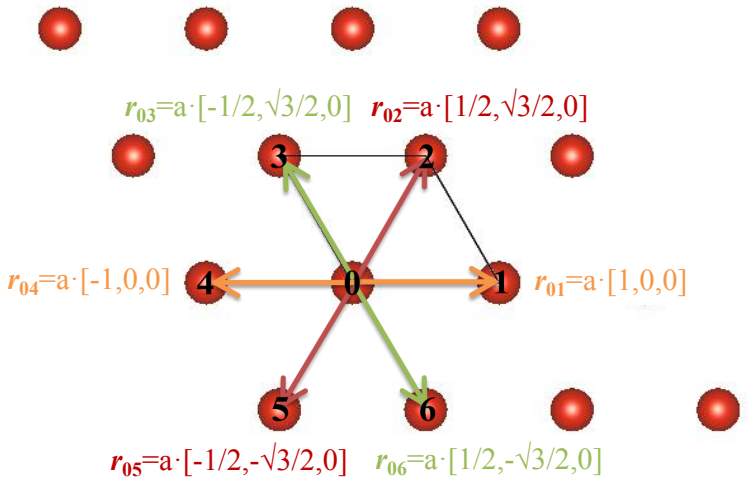

Figure S6: Schematic diagram of six pairs of the nearest neighbor DMI within VSi_2N_4 derivatives.

in which $\boldsymbol{d}_{ij}$ is the DMI vector quantifying the strength and chirality and expressed as $\boldsymbol{d}_{ij} = d^{\parallel}(\boldsymbol{r}_{ij} \times \boldsymbol{e}_z) + d^z \boldsymbol{e}_z$, $\boldsymbol{S}_{i(j)}$ is the unit vector of spin moment at position $\boldsymbol{r}_{i(j)}$. Previous studies have shown that the non-SOC spin spiral dispersions are degenerate, while the spin spiral dispersions including SOC become asymmetric.[11,12] To obtain the DMI parameters between two adjacent V atoms, we implement the qSO method based on generalized Bloch theorem and treat SOC within the first-order perturbation theory.[11–19] The homogeneous spin spiral $\boldsymbol{S}_i = [\sin(\boldsymbol{q} \cdot \boldsymbol{r}_i), 0, \cos(\boldsymbol{q} \cdot \boldsymbol{r}_i)]$ is adopted with $\boldsymbol{q}$ being a spin spiral vector in the x-z plane. It has been proven that only the $d_{ij}^{\parallel}$ components from each pair contribute to $E_{\mathrm{DM}}^{\parallel}$, then the system energy functional of $\boldsymbol{q}$ is expressed as

$$E_{\mathrm{DM}}^{\parallel}(\boldsymbol{q}) = d_{ij}^{\parallel} \sum_{\langle i,j \rangle} r_{ij}^{1} \sin(\boldsymbol{q} \cdot \boldsymbol{r}_{ij}), \tag{S5}$$

where r_{ij}^{1} represents the 1 direction component of $\boldsymbol{r}_{ij}$. For a hexagonal lattice with the $\boldsymbol{q}$ vector propagating along the $\Gamma - K$ direction of the reciprocal space ($\boldsymbol{q} = \frac{2\pi}{a} q \left[\frac{1}{2}, \frac{\sqrt{3}}{2}, 0\right]$), the in-plane components of respective DMI energy can be further expressed by

$$\Delta E_{\mathrm{DM}}^{\parallel}(\boldsymbol{q}) = \frac{E(\boldsymbol{q}) - E(-\boldsymbol{q})}{2} = d_{ij}^{\parallel} \sum_{\langle i,j \rangle} r_{ij}^{1} \sin(\boldsymbol{q} \cdot \boldsymbol{r}_{ij}), \tag{S6}$$

Accumulating the energy contributions from six exchange pairs of the nearest neighbors in Fig. S6 gives the relation:

$$\Delta E_{\mathrm{DM}}^{\parallel}(\boldsymbol{q}) = d^{\parallel} \boldsymbol{q} \cdot (\boldsymbol{r}_{01} + \boldsymbol{r}_{02} + \boldsymbol{r}_{03} + \boldsymbol{r}_{04} + \boldsymbol{r}_{05} + \boldsymbol{r}_{06}) = d^{\parallel} \frac{3a}{2} \frac{2\pi}{a} q. \tag{S7}$$

To investigate $d_{\parallel}$ for Janus VA_2Z_4 monolayer, we calculate a SOC-induced spin spiral rotating in the x-z plane as shown in the upper panels of Fig. S7.[12,16,17] The respective DMI energy $\Delta E_{\mathrm{DM}}[q]$ for $d_{\parallel}$ are determined by $\Delta E_{\mathrm{DM}}[q] = (E[q] - E[-q])/2$, which are shown in the lower panels of Fig S7. In the interval between $q = \pm 0.1(\frac{2\pi}{a})$, $\Delta E_{\mathrm{DM}}[q]$ shows a good linear relationship with q as

$$\Delta E_{\mathrm{DM}}^{\parallel}(\boldsymbol{q}) \propto D \frac{2\pi}{a} q, \tag{S8}$$

in which D is DMI parameter. By fitting D in the lower panels of Fig. S7 and combining Eqs. S7 and S8, we can get the $d^y = 2D/3a$ for the Janus VA_2Z_4 monolayers.

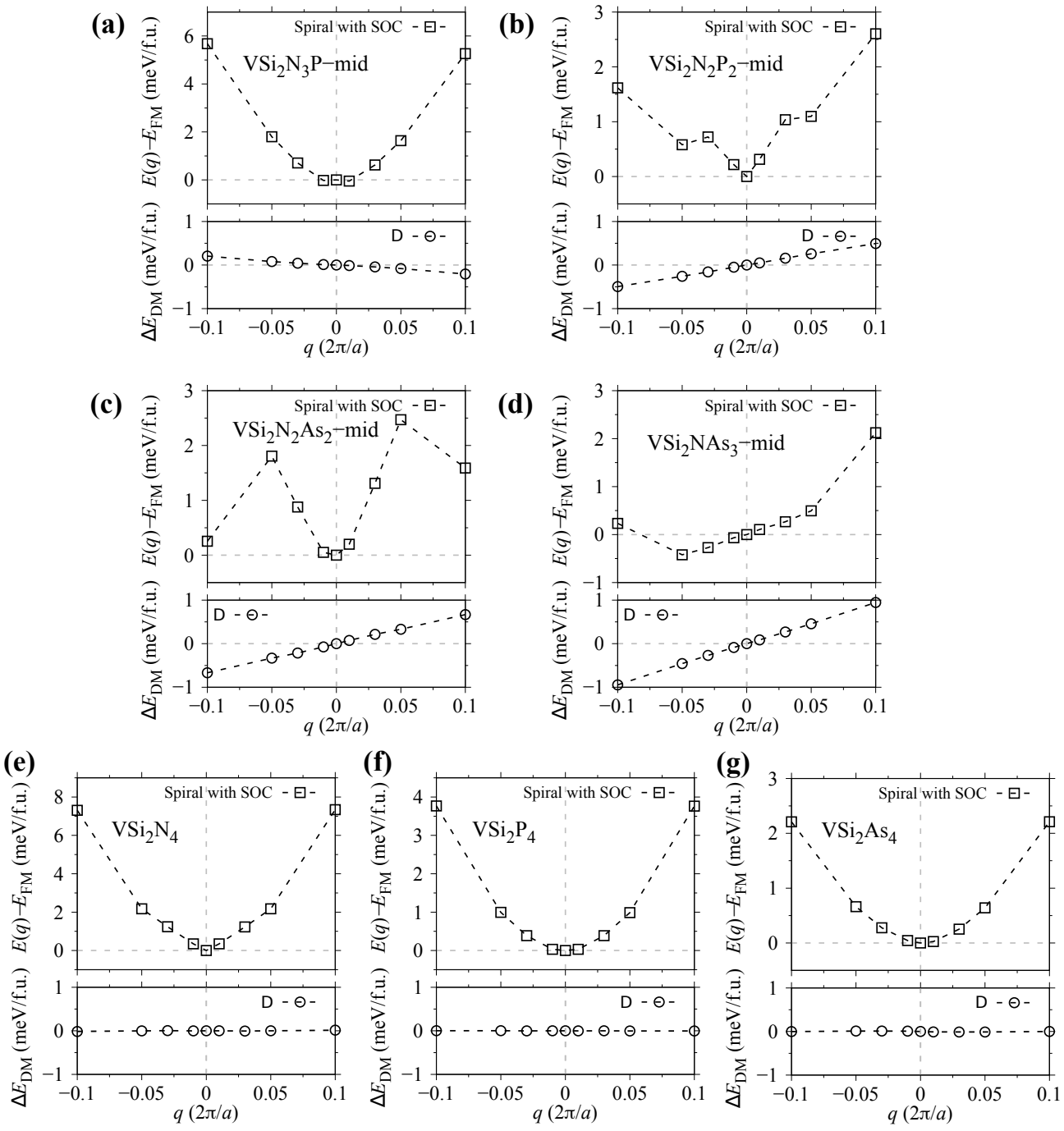

Figure S7: Calculated SOC-included spin-spiral energy $\Delta E(q)$ rotating in x-z plane (upper panels) and the respective DMI energy $\Delta E_{\mathrm{DM}}(q)$ (lower panels) as functions of spiral vector length q along the $\Gamma - K$ direction, plotted for (a) VSi_2N_3P-mid, (b) $VSi_2N_2P_2$-mid, (c) $VSi_2N_2As_2$-mid, (d) VSi_2NAs_3-mid, (e-g) VSi_2Z_4 (Z = N, P, As). $\Delta E(q)$ is given with respect to the ferromagnetic state at $q = 0$.

Calculation method of topological charge Q

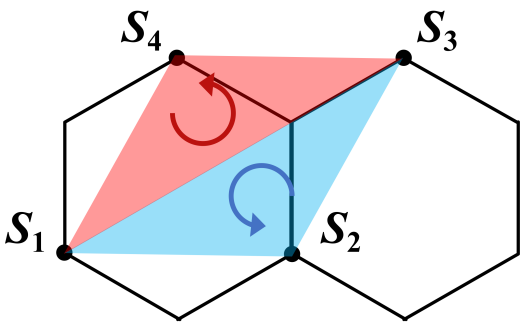

Figure S8: Honeycomb lattice showing spins $\boldsymbol{S}_i$ $(i = 1, 2, 3, 4)$ following a counter-clockwise order on each triangle grid.

In the continuum case, the non-trivial topological magnetic textures can be characterized by the topological charge defined as[20–22]

$$Q = \frac{1}{4\pi} \int \boldsymbol{S} \cdot \left(\frac{\partial \boldsymbol{S}}{\partial x} \times \frac{\partial \boldsymbol{S}}{\partial y} \right) dxdy, \tag{S9}$$

where $\boldsymbol{S}$ is a normalized magnetization vector. In this case, Q is only well-defined where all the spins are approximately parallel to neighbors, and the ferromagnetic state can be distinguished from other non-trivial states. For the convenience of calculations, a lattice model that partitions the spins into nearest neighbor triangles is adopted, and the charge can be described as[20,23–25]

$$Q = \frac{1}{4\pi} \sum_{\Omega} \left[\Omega(\boldsymbol{S}_1, \boldsymbol{S}_2, \boldsymbol{S}_3) + (\boldsymbol{S}_1, \boldsymbol{S}_3, \boldsymbol{S}_4) \right]. \tag{S10}$$

Here $\Omega(\boldsymbol{S}_1, \boldsymbol{S}_2, \boldsymbol{S}_3)$ denotes the signed area of the spherical triangle with corner $\boldsymbol{S}_1$, $\boldsymbol{S}_2$, $\boldsymbol{S}_3$. $4\pi Q$ is the total signed area of a surface, which is obtained by gluing all elementary spherical triangles with corners $\boldsymbol{S}_1$, $\boldsymbol{S}_2$, $\boldsymbol{S}_3$ (the blue triangle in Fig. S8) and $\boldsymbol{S}_1$, $\boldsymbol{S}_3$ (the red triangle in Fig. S8), $\boldsymbol{S}_4$, respectively. An explicit formula to compute the signed area Ω with unit spin vector is

$$\exp\left(i \frac{\Omega(\boldsymbol{S}_1, \boldsymbol{S}_2, \boldsymbol{S}_3)}{2} \right) = \rho^{-1} \left[1 + \boldsymbol{S}_1 \cdot \boldsymbol{S}_2 + \boldsymbol{S}_2 \cdot \boldsymbol{S}_3 + \boldsymbol{S}_3 \cdot \boldsymbol{S}_1 + i \boldsymbol{S}_1 \cdot (\boldsymbol{S}_2 \times \boldsymbol{S}_3) \right], \tag{S11}$$

where $-2\pi < \Omega < 2\pi$ and $\rho = \left[2 \left(1 + \boldsymbol{S}_1 \cdot \boldsymbol{S}_2 \right) \left(1 + \boldsymbol{S}_2 \cdot \boldsymbol{S}_3 \right) \left(1 + \boldsymbol{S}_3 \cdot \boldsymbol{S}_1 \right) \right]^{1/2}$. Converting the above complex exponential form to its corresponding trigonometric function form, one can obtain

$$\tan\left(\frac{\Omega(\boldsymbol{S}_1, \boldsymbol{S}_2, \boldsymbol{S}_3)}{2} \right) = \frac{\boldsymbol{S}_1 \cdot (\boldsymbol{S}_2 \times \boldsymbol{S}_3)}{1 + \boldsymbol{S}_1 \cdot \boldsymbol{S}_2 + \boldsymbol{S}_2 \cdot \boldsymbol{S}_3 + \boldsymbol{S}_3 \cdot \boldsymbol{S}_1}. \tag{S12}$$

So that the previous equation can be written as

$$Q = \frac{1}{4\pi} \sum_{\Omega} \left[\tan^{-1} \left(\frac{\boldsymbol{S}_1 \cdot (\boldsymbol{S}_2 \times \boldsymbol{S}_3)}{1 + \boldsymbol{S}_1 \cdot \boldsymbol{S}_2 + \boldsymbol{S}_2 \cdot \boldsymbol{S}_3 + \boldsymbol{S}_3 \cdot \boldsymbol{S}_1} \right) + \tan^{-1} \left(\frac{\boldsymbol{S}_1 \cdot (\boldsymbol{S}_3 \times \boldsymbol{S}_4)}{1 + \boldsymbol{S}_1 \cdot \boldsymbol{S}_3 + \boldsymbol{S}_3 \cdot \boldsymbol{S}_4 + \boldsymbol{S}_4 \cdot \boldsymbol{S}_1} \right) \right] \tag{S13}$$

It takes the topological charge of $Q = \pm 1$ for skyrmions and antiskyrmions, signifying their whole-wound nature. The topological charge of merons and antimerons, on the other hand, is $Q = \pm 1/2$ due to their half-wound structures. However, the topological charge integral is $Q = \pm 1$ when the center radial symmetric distribution of the bimeron is taken into account.

Calculation method of TMTs-mediated MCE

An *ab-initio* informed spin Hamiltonian model is utilized to investigate the dynamics of magnetic spins in Janus monolayers. The Hamiltonian is expressed as

$$H = -\frac{1}{2}\sum_{<i,j>} J(\mathbf{s}_i \cdot \mathbf{s}_j) - \frac{1}{2}\sum_{<i,j>} \boldsymbol{d}_{ij} \cdot (\mathbf{s}_i \times \mathbf{s}_j) - K_u \sum_i (\mathbf{s}_i \cdot \mathbf{e}_i)^2 - \sum_i \mu_s \mathbf{s}_i \cdot (\mathbf{H}_{\mathrm{app}} + \mathbf{H}_{\mathrm{dp}}), \tag{S14}$$

where $\mathbf{s}_i$ and $\mathbf{s}_j$ are the spin unit vectors of each atoms at sites i and j, respectively. J and $\boldsymbol{d}_{ij}$ represent the Heisenberg exchange interaction and DMI interaction vector, characterizing the symmetric and asymmetric interactions between two nearest localized spins. K_u, $\mathbf{e}_i$, and μ_s represent the magnetocrystalline anisotropy energy, the easy axis vector, and the magnetic moment at atom i, respectively. $\mathbf{H}_{\mathrm{app}}$ and $\mathbf{H}_{\mathrm{dp}}$ are the external and demagnetization fields, respectively. The magnetic parameters of J, $\boldsymbol{d}_{ij}$, and K_u are derived from *ab-initio* calculations. To address the spatial and temporal evolution of atomic spins under external fields and thermal fluctuations, spin dynamics simulations are utilized to model the behavior of localized magnetic moments. The time-dependent spin direction is governed by the atomistic Landau–Lifshitz–Gilbert (LLG) equation as

$$\frac{\partial \mathbf{s}_i}{\partial t} = -\frac{\gamma}{(1+\lambda^2)}[\mathbf{s}_i \times \mathbf{H}^i_{\mathrm{eff}} + \lambda \mathbf{s}_i \times (\mathbf{s}_i \times \mathbf{H}^i_{\mathrm{eff}})], \tag{S15}$$

where the effective field on each spin denoted as $\mathbf{H}^i_{\mathrm{eff}}$ is derived from the spin Hamiltonian as $\mathbf{H}^i_{\mathrm{eff}} = -\partial H/\partial \mathbf{s}_i + \mathbf{H}^i_{\mathrm{th}}$. The fluctuating thermal field $\mathbf{H}^i_{\mathrm{th}}$ is introduced via a Langevin dynamic approach, simulating the interaction of the system with a heat bath. Simulations are conducted on a 100 × 100 × 1 supercell with in-plane periodic boundary conditions. VAMPIRE is used for Monte Carlo and spin dynamics simulations with 100,000 equilibration and 100,000 averaging steps.[1,2] Additionally, the self-induced demagnetization field due to atomic spins is taken into account, enabling the accurate simulation of temperature-dependent magnetization behavior.

The figures of merit for evaluating MCE, such as the isothermal magnetic entropy change (ΔS_{M}) and the adiabatic temperature change (ΔT_{ad}), can be derived from the first law of thermodynamics and Maxwell's thermodynamic relations.[3] ΔS_{M} is expressed as

$$\Delta S_{\mathrm{M}} = \int_0^H \left(\frac{\partial S}{\partial H}\right)_T \mathrm{d}H = \mu_0 \int_0^H \left(\frac{\partial M}{\partial T}\right)_H \mathrm{d}H, \tag{S16}$$

and ΔT_{ad} is given by

$$\Delta T_{\mathrm{ad}} = -\int_0^H \frac{T}{\rho c_{\mathrm{p}}} \left(\frac{\partial S}{\partial H}\right)_T \mathrm{d}H = -\mu_0 \int_0^H \frac{T}{\rho c_{\mathrm{p}}} \left(\frac{\partial M}{\partial T}\right)_H \mathrm{d}H, \tag{S17}$$

where S is entropy, M is magnetization, μ_0 is vacuum permeability, H is magnetic field, ρ is the density, and c_{p} is the specific heat capacity.

Formation and annihilation of TMTs

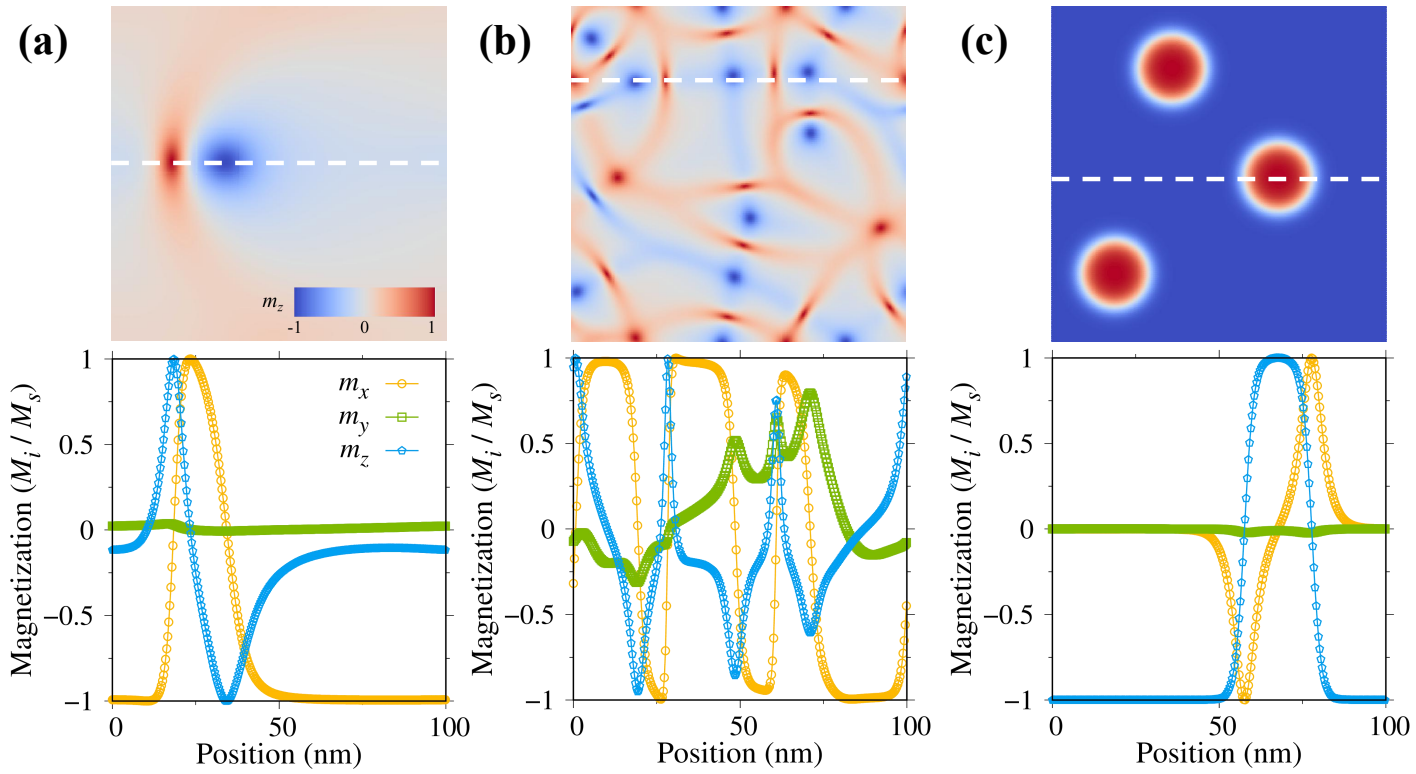

Figure S9: Topological magnetic textures of (a) $VSi_2N_2P_2$, (b) $VSi_2N_2As_2$, and (c) VSi_2NAs_3 after reaching 0 K, and the path changes of the magnetization components along the top-row subfigures.

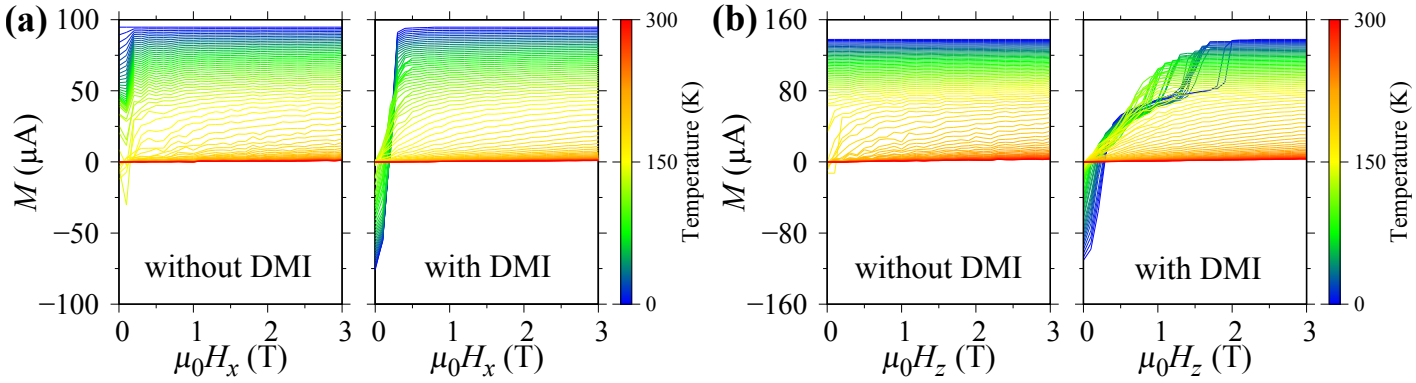

Figure S10: Isothermal magnetization curves, with and without consideration of DMI for (a) $VSi_2N_2P_2$ and (b) VSi_2NAs_3, calculated at different temperatures with magnetic fields applied along the positive directions.

References

(1) Evans, R. F.; Fan, W. J.; Chureemart, P.; Ostler, T. A.; Ellis, M. O.; Chantrell, R. W. Atomistic spin model simulations of magnetic nanomaterials. *Journal of Physics: Condensed Matter* **2014**, *26*, 103202.

(2) Wang, Q. H. et al. The magnetic genome of two-dimensional van der Waals materials. *ACS Nano* **2022**, *16*, 6960–7079.

(3) Franco, V.; Blázquez, J.; Ipus, J.; Law, J.; Moreno-Ramírez, L.; Conde, A. Magnetocaloric effect: From materials research to refrigeration devices. *Progress in Materials Science* **2018**, *93*, 112–232.

(4) Wang, L.; Shi, Y.; Liu, M.; Zhang, A.; Hong, Y. L.; Li, R.; Gao, Q.; Chen, M.; Ren, W.; Cheng, H. M.; Li, Y.; Chen, X. Q. Intercalated architecture of MA_2Z_4 family layered van der Waals materials with emerging topological, magnetic and superconducting properties. *Nature Communications* **2021**, *12*, 2361.

(5) Blöchl, P. E. Projector augmented-wave method. *Physical Review B* **1994**, *50*, 17953–17979.

(6) Kresse, G.; Furthmüller, J. Efficiency of *ab-initio* total energy calculations for metals and semiconductors using a plane-wave basis set. *Computational Materials Science* **1996**, *6*, 15–50.

(7) Kresse, G.; Furthmüller, J. Efficient iterative schemes for *ab initio* total-energy calculations using a plane-wave basis set. *Physical Review B* **1996**, *54*, 11169–11186.

(8) Kresse, G.; Joubert, D. From ultrasoft pseudopotentials to the projector augmented-wave method. *Physical Review B* **1999**, *59*, 1758–1775.

(9) Perdew, J. P.; Burke, K.; Ernzerhof, M. Generalized Gradient Approximation Made Simple. *Physical Review Letters* **1996**, *77*, 3865–3868.

(10) He, W.; Yin, Y.; Tang, Z.; Wang, X.; Yuan, H.; Gong, Q.; Yi, M. Mechanically strong and room-temperature magnetocaloric monolayer VSi_2N_4 semiconductor. *Applied Physics Letters* **2024**, *125*, 022407.

(11) Liang, J.; Cui, Q.; Yang, H. Electrically switchable Rashba-type Dzyaloshinskii-Moriya interaction and skyrmion in two-dimensional magnetoelectric multiferroics. *Physical Review B* **2020**, *102*, 220409.

(12) Li, P.; Yu, D.; Liang, J.; Ga, Y.; Yang, H. Topological spin textures in 1T-phase Janus magnets: Interplay between Dzyaloshinskii-Moriya interaction, magnetic frustration, and isotropic higher-order interactions. *Physical Review B* **2023**, *107*, 54408.

(13) Heide, M.; Bihlmayer, G.; Blügel, S. Describing Dzyaloshinskii-Moriya spirals from first principles. *Physica B: Condensed Matter* **2009**, *404*, 2678–2683.

(14) Sandratskii, L. M. Insight into the Dzyaloshinskii-Moriya interaction through first-principles study of chiral magnetic structures. *Physical Review B* **2017**, *96*, 024450.

(15) Jiang, J.; Liu, X.; Li, R.; Mi, W. Topological spin textures in a two-dimensional $MnBi_2(Se, Te)_4$ Janus material. *Applied Physics Letters* **2021**, *119*, 072401.

(16) Ga, Y.; Cui, Q.; Liang, J.; Yu, D.; Zhu, Y.; Wang, L.; Yang, H. Dzyaloshinskii-Moriya interaction and magnetic skyrmions induced by curvature. *Physical Review B* **2022**, *106*, 054426.

(17) Li, P.; Cui, Q.; Ga, Y.; Liang, J.; Yang, H. Large Dzyaloshinskii-Moriya interaction and field-free topological chiral spin states in two-dimensional alkali-based chromium chalcogenides. *Physical Review B* **2022**, *106*, 24419.

(18) Cui, Q.; Zhu, Y.; Ga, Y.; Liang, J.; Li, P.; Yu, D.; Cui, P.; Yang, H. Anisotropic Dzyaloshinskii-Moriya interaction and topological magnetism in two-dimensional magnets protected by $P\bar{4}m2$ crystal symmetry. *Nano Letters* **2022**, *22*, 2334–2341.

(19) Jiang, J.; Ga, Y.; Li, P.; Cui, Q.; Wang, L.; Yu, D.; Liang, J.; Yang, H. Origami-driven Dzyaloshinskii-Moriya interaction in centrosymmetric two-dimensional magnets. *Physical Review B* **2024**, *109*, 014402.

(20) Augustin, M.; Jenkins, S.; Evans, R. F.; Novoselov, K. S.; Santos, E. J. Properties and dynamics of meron topological spin textures in the two-dimensional magnet $CrCl_3$. *Nature Communications* **2021**, *12*, 185.

(21) Dou, K.; He, Z.; Du, W.; Dai, Y.; Huang, B.; Ma, Y. d^0 Magnetic Skyrmions in Two-Dimensional Lattice. *Advanced Functional Materials* **2023**, *33*, 2301817.

(22) Yoshimochi, H.; Takagi, R.; Ju, J.; Khanh, N. D.; Saito, H.; Sagayama, H.; Nakao, H.; Itoh, S.; Tokura, Y.; Arima, T.; Hayami, S.; Nakajima, T.; Seki, S. Multistep topological transitions among meron and skyrmion crystals in a centrosymmetric magnet. *Nature Physics 2024* **2024**, *20*, 1001–1008.

(23) Berg, B.; Lüscher, M. Definition and statistical distributions of a topological number in the lattice O(3) σ-model. *Nuclear Physics B* **1981**, *190*, 412–424.

(24) Rózsa, L.; Simon, E.; Palotás, K.; Udvardi, L.; Szunyogh, L. Complex magnetic phase diagram and skyrmion lifetime in an ultrathin film from atomistic simulations. *Physical Review B* **2016**, *93*, 024417.

(25) Yin, G.; Li, Y.; Kong, L.; Lake, R. K.; Chien, C. L.; Zang, J. Topological charge analysis of ultrafast single skyrmion creation. *Physical Review B* **2016**, *93*, 174403.